

pubs.acs.org/JPCC Article

# Thickness-Dependent Exciton Dynamics in Thermally Evaporated Rubrene Thin Films

Published as part of The Journal of Physical Chemistry virtual special issue "Josef Michl Festschrift".

Chia-Hsun Chen, Pin-Hao Sher, Cheng-Pin Chen, Wing-Kit Choi, Christopher J. Bardeen, Tien-Lung Chiu,\* Juen-Kai Wang,\* and Jiun-Haw Lee\*



Cite This: J. Phys. Chem. C 2020, 124, 25729–25737



ACCESS More Article Recommendations Supporting Information

Supporting Information

Thickness 0.01

ABSTRACT: In this study, exciton dynamics and singlet fission (SF) in amorphous rubrene thin films with various thicknesses from 5 to 100 nm were investigated. No clear X-ray diffraction peaks could be observed from these thin films, and their absorption and photoluminescence (PL) spectra were similar, although the PL slightly red-shifted with increasing rubrene thickness. However, temperature-dependent and time-resolved PL measurements showed dramatic differences between 5 and 100 nm thick films. There were two different relaxation channels in a 100 nm rubrene film, one of which is fission capable (channel a) and the other fission inactive (channel b). The SF process of species a was endothermic with activation energy 58 meV, as determined by time-resolved PL measurements carried out over a temperature range 300-77 K. On the other hand, for a 5 nm rubrene thin film, both this endothermic SF route and a weaker, exothermic SF channel below 160 K were observed with a SF rate of 0.22 ns<sup>-1</sup>. This was attributed to a new fission channel (channel c) that is probably due to molecular packing in the beginning of film growth. Channel c indicated a lower coupling molecular strength together with higher singlet energy that compensated the required thermal energy barrier for SF. A phase transition from amorphous to polycrystalline rubrene was observed when a thermal annealing treatment was applied to the 100 nm rubrene film. The PL spectral profile was dominated by microcrystals oriented with the crystal c-axis parallel with the substrate, and these high density of SF "hotspots" increased the SF rate with only a weak temperature dependence from 120 to 300 K.

## INTRODUCTION

Singlet fission (SF), the multiexciton generation process which splits one singlet exciton into two triplet excitons, has attracted extensive research interest owing to applications in photovoltaic (PV) devices and organic light-emitting diodes (OLEDs). In a PV device, photon energy higher than the optical bandgap experiences a thermalization process which is one of the major energy-loss issues limiting the power conversion efficiency. By using SF materials, one photon generates two electron—hole pairs to achieve an internal quantum yield (IQE) over 100%, which has the potential to surpass Shockley—Queisser limit. In addition, SF materials can be also applied for OLEDs for obtaining production efficiency of exciton over 100%. Polyacene molecular crystal exhibit efficient SF rates on the range 0.1—300 ps. 10—12 The local details of the molecular packing in polyacene materials is

believed to greatly affect the SF efficiency. <sup>13–15</sup> Piland et al. reported that polycrystalline tetracene had faster SF with decay times of 70–90 ps as compared to about 250 ps for a single crystal, which was attributed to the existence of face to face defects or packing motifs in the polycrystalline film. <sup>16</sup> After the polycrystalline samples were annealed to generate a single-crystal phase, less rapid SF was observed due to improved herringbone packing.

Received: August 29, 2020 Revised: October 17, 2020 Published: November 9, 2020





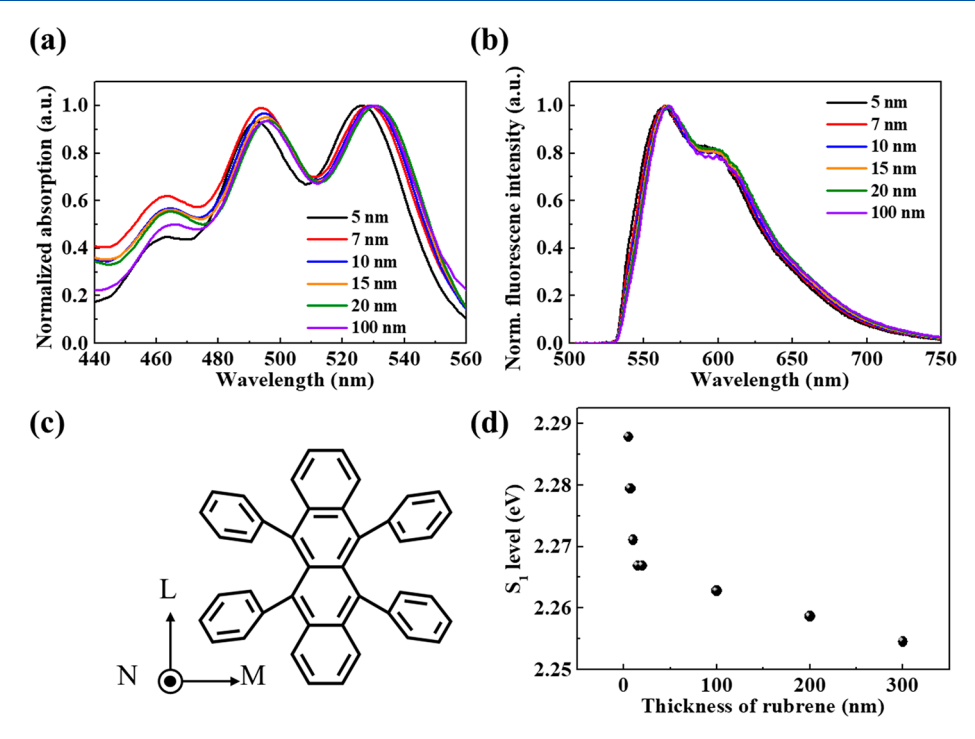


**Figure 1.** Normalized (a) absorption and (b) PL spectra of rubrene thin films with thickness of 5, 7, 10, 15, 20, and 100 nm at *T* of 300 K. (c) Molecular structure of rubrene. (d) S<sub>1</sub> level variations with various rubrene thicknesses.

5,6,11,12-Tetraphenyltetracene (rubrene), a derivative of tetracene attached with four phenyl rings, tends to grow in an amorphous phase under thermal evaporation, which is widely used for OLED applications.<sup>17</sup> Compared to tetracene and pentacene, excimer formation in rubrene is greatly suppressed. In addition, rubrene exhibits a high fluorescence quantum yield close to 100% in solution, which leaves SF as the major nonradiative channel in the solid state. Park et al. found that after 60-80 °C thermal annealing, amorphous rubrene transformed into crystalline domains, forming disk-shaped aggregates with hundreds of micrometer diameter and roughness of approximate 10 nm. 18-21 Lin et al. annealed a rubrene/C<sub>60</sub> bilayer to shift the charge transfer state which benefited triplet exciton harvesting.<sup>22</sup> Interestingly, rubrene films can be grown either in the bulk crystalline phase or with very low short-range order by molecular beam epitaxy. 23,24 The ability to produce different packing motifs using the same molecule presents an opportunity to study how the morphology of rubrene influences the exciton dynamics and SF, both of which will impact the eventual device performances.25

In most cases, the photophysical behavior of a sample should be determined by purely local molecular interactions on length scales much less than 5 nm, so we would not expect different film thicknesses to affect the excited state dynamics. In this paper, we tested this assumption by investigating the exciton dynamics of ordinary amorphous rubrene thin films with various thicknesses (5-100 nm) which were deposited by using thermal evaporation. Here, "amorphous" means no clear crystallinity that can be detected by X-ray diffraction (XRD) measurements. With increasing rubrene thickness, redshifts in absorption and photoluminescence (PL) spectra were observed, which indicated a decrease in singlet  $(S_1)$  energy due to molecular packing. Temperature-dependent PL spectra showed similar trends (blue shift and intensity decrease) with increasing temperature (T) for various rubrene thicknesses.

However, the changes in PL peak intensity and spectral profile were significant in the 100 nm film compared to that of the 5 nm one, indicating different molecular packings. For a 100 nm rubrene film, spectral changes, together with a 19.7× PL intensity enhancement when the temperature was decreased from 300 to 77 K, indicated one relaxation channel which was fission capable. In time-resolved PL (TRPL) measurements of the 100 nm rubrene film, the endothermic SF process was characterized with activation energy 58 meV due to fission capable site (channel a). In the case of a 5 nm rubrene film, in addition to the endothermic SF channel a, a second exothermic SF (SF rate,  $k_{-2} = 0.22 \text{ ns}^{-1}$ ) channel c was observed and attributed to a different molecular packing with a higher singlet energy (S<sub>1</sub>). After thermal annealing (120 °C for 12 h), the 100 nm rubrene thin film was transformed from amorphous to polycrystalline, which could be detected using polarized optical microscopy (POM) and XRD patterns. In contrast, no change in the 5 nm rubrene film was observed. Temperature-dependent PL and TRPL spectra of the 100 nm rubrene film showed a greater SF rate in the polycrystalline film compared to that in the amorphous one. Therefore, a diffusion-mediated SF process was proposed to explain these variations in temperature-dependent PL spectral profiles. The sensitivity of SF to film morphology has also been observed in tetracene and may be a general feature of the polyacenes.<sup>26</sup>

# **■ EXPERIMENTAL SECTION**

**Sample Fabrication.** An 80 nm lithium fluoride layer was first deposited on a glass substrate as a singlet blocking layer, followed by deposition of an amorphous rubrene thin film using a thermal evaporator under ultrahigh vacuum  $(1\times 10^{-6}~{\rm Torr})^{27}$  After deposition, thin-film samples were transferred directly to a nitrogen glovebox with oxygen levels under 0.5 ppm and then encapsulated with a cover glass by UV glue. Layer thicknesses and deposition rate were carefully monitored

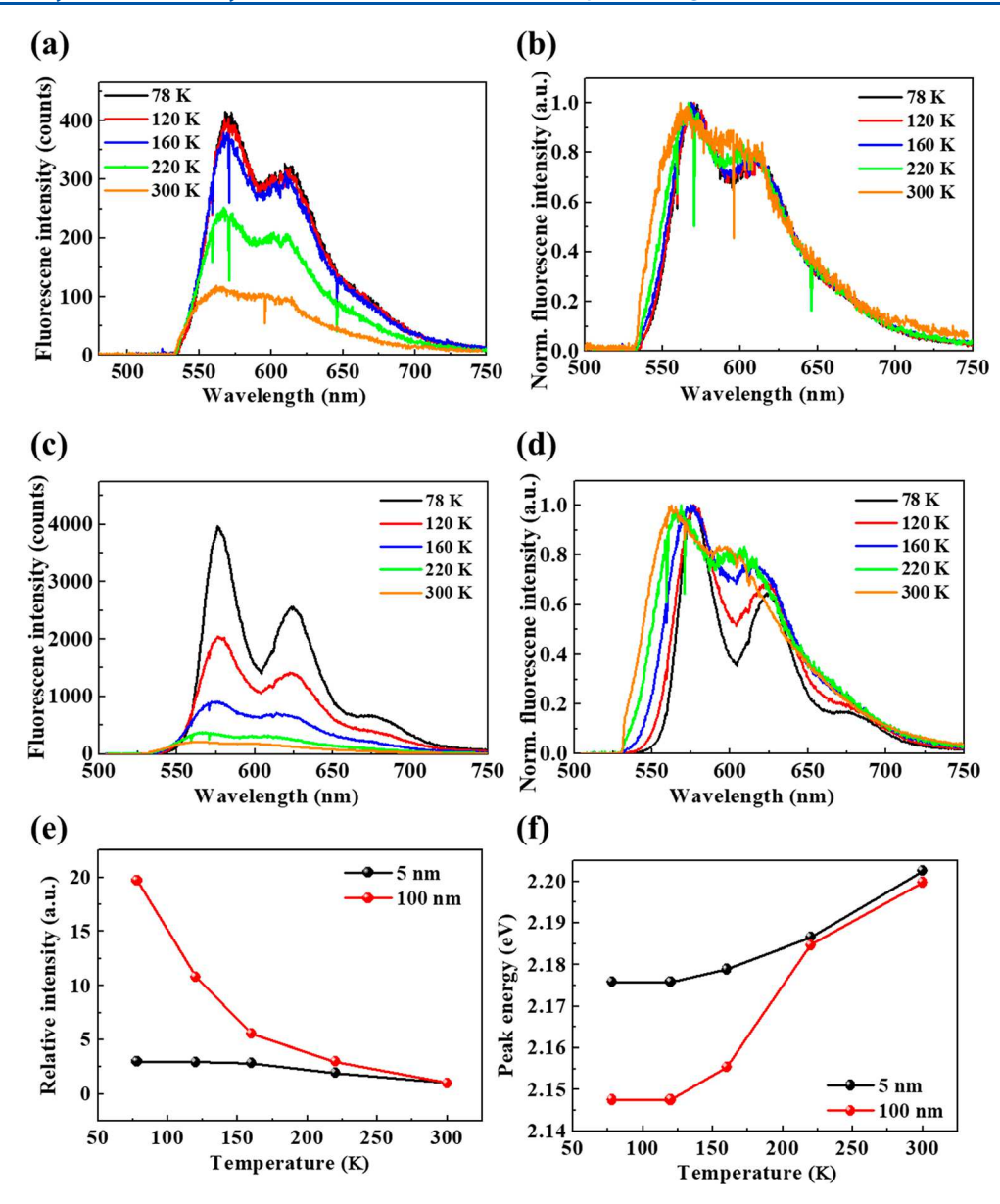


Figure 2. Temperature-dependent (a and c) PL spectra, (b and d) normalized PL spectra, (e) PL intensity (normalized by 300 K), and (f) PL peak wavelength of 5 and 100 nm rubrene thin films under 78, 120, 160, 220, and 300 K.

by a Maxtek 350 quartz crystal microbalance. For thermal annealing, a hot plate was employed to perform thermal treatment with precise temperature control. The annealing process used the encapsulated samples. AFM samples were fabricated as the same process on silicon substrates ( $R_{\rm q}=0.59$  nm) without encapsulation. To investigate the morphology of rubrene thin films, atomic force microscopy (AFM, Vecco Bio-Scope) with tapping mode was used.

**Optical Characterization.** Steady state absorption and fluorescence spectra were recorded using Hitachi U4100 and F4500 instruments, respectively. A polarized light microscope (PLM, NIKON H550s) was employed to identify the spherulitic disks created by rubrene crystallization. Exciton dynamics at various temperatures were measured by TRPL with a 10× objective (MPLFLN-BD, Olympus). The excitation pulses were supplied by a 532 nm Nd:VAN laser source (High Q IC-1064–15000), which was doubled frequency from 1064 nm, and a RF acoustic pulse selector (pulseSelect, APE, 170 kHz). By using a spatial filter, half wave plate, and broad band

polarizer (SM1PM10), the laser frequency noise can be eliminated and its intensity can be precisely adjusted. An excitation density of  $1 \times 10^{15} \text{ cm}^{-3}$  was employed, which has been proven to prevent nonlinear effects such as singletsinglet annihilation (SSA).<sup>12</sup> The instrument response of the system was 123 ps. Samples were placed in a cryostat (Cryo Industries CFM 1738-X6M102, 5119) to vary the temperature from 78 (liquid nitrogen) to 300 K. After the rubrene thin film was excited by a laser pulse, steady state fluorescence spectra were recorded by a charge-coupled device (CCD, Andor DU920P BR-DD) and time-resolved data were collected using a time-correlated single photon counting (TCSPC) system. All the fluorescence decays in the main text were integrated over all emitting wavelengths, and the wavelength dependent fluorescence decays in the Supporting Information were collected by using a monochromator (Horiba Jobin Yvon MicroHR) before the TCSPC system. The XRD patterns were measured with an X-ray diffractometer (Cu K $\alpha$  radiation,  $\lambda$  = 1.54 Å, Bruker D8 DISCOVER SSS Multi Function High

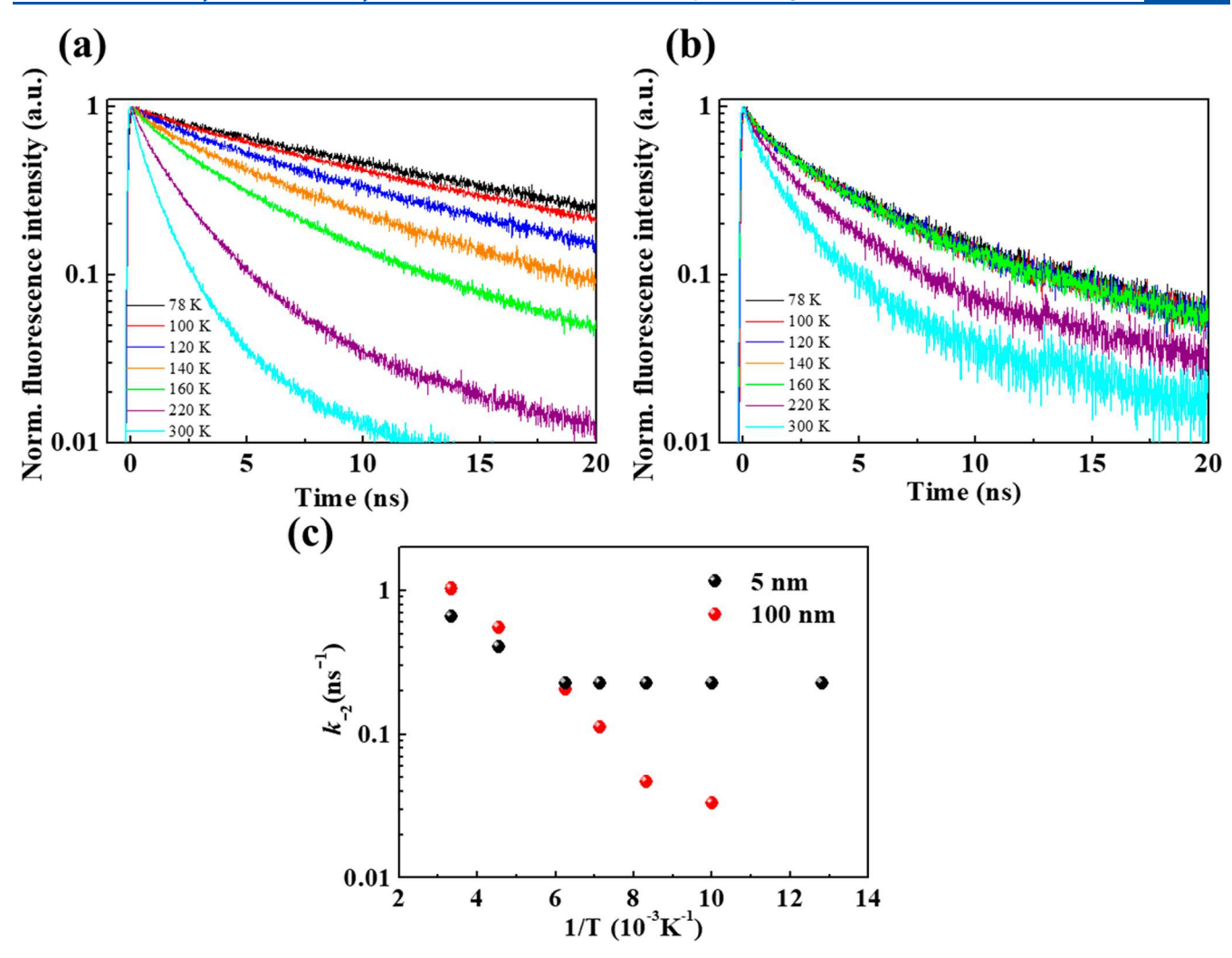


Figure 3. TRPL signals of (a) 100 nm and (b) 5 nm rubrene thin films with T of 78–300 K. (c) SF rates with Arrhenius plot and (d) illustrated kinetic model with species a and c for 5 and 100 nm rubrene thin films.

Power XRD) under 40 kV and 100 mA tube current. The X-ray profiles were recorded from 5 to  $30^{\circ}$  in steps of  $0.05^{\circ}$ , with an incident angle of  $0.3^{\circ}$ .

### RESULTS AND DISCUSSION

Normalized absorption and PL spectra of rubrene thin films with various thicknesses of 5, 7, 10, 15, 20, and 100 nm are shown in parts a and b of Figure 1, respectively. Figure 1c shows the molecular structure of rubrene and its defined axes. In Figure 1a, the lowest excitation band with peak around 530 nm originates from the S<sub>0</sub> to S<sub>1</sub> transition along the rubrene M axis. Higher energy absorption peaks have transition dipoles oriented along the N and L axes.<sup>28</sup> With increasing film thickness, both the absorption and PL spectra exhibit a slight redshift. In parts a and b of Figure 1, except for the small spectral redshift, the spectral profiles are almost identical, indicating that all the films are amorphous with no phase transition for increasing thickness. 10 The vibronic features of the PL spectra are similar to the PL line shape of isolated molecules dissolved in toluene, and the amorphous nature is also confirmed by powder-XRD patterns, which do not show any signature crystal peaks (Supporting Information, Figure S1).<sup>29</sup> The S<sub>1</sub> energy of each layer thickness can be deduced from the crossing point of the absorption and PL spectra (Figure S2) and are displayed in Figure 1d.30 As the thickness

increases from 5 to 20 nm, the  $S_1$  energy abruptly decreases 0.021 eV from 2.288 to 2.267 eV with a slope of -1.3 meV/nm. Toward 300 nm, the  $S_1$  energy further decreases by 0.012 eV to 2.255 eV with a linear slope of -0.043 meV/nm. For the limiting cases of noncrystalline (solution) and perfect crystalline (single crystal), the  $S_1$  energies are 2.29 and 2.23 eV, respectively. Hence, one can deduce that the PL of the 5 nm thin film originates from monomers that have only weak coupling to their neighbors. In the 100 and 300 nm films, the shift to lower energies is evidence of higher interactions with neighboring molecules, at least in the form of a higher local dielectric. But overall, the changes in the steady-state spectra are quite small, consistent with the idea that the films should behave similarly in terms of their photophysics.

The behavior of the different thickness films begins to diverge when their temperature dependent spectra are measured. PL spectra of 5- and 100 nm rubrene thin films were recorded at temperatures of 78, 120, 160, 220, and 300 K as shown in Figure 2. Parts a and b of Figure 2 show the temperature-dependent PL and normalized PL spectra of 5 nm rubrene thin film. Parts c and d of Figure 2 show the temperature-dependent PL and normalized PL results of 100 nm case. No spectral shift can be observed in the temperature-dependent absorption spectra of individual 5 and 100 nm rubrene films (Figure S3), indicating that the dielectric and

Table 1. Temperature-Dependent Fitting Parameters of 5 and 100 nm Rubrene Thin Films

	100 nm film				5 nm film				
temperature (K)	$k_{-2} (ns^{-1})$	Φ <sub>2a</sub> (%)	$\Phi_{\rm r}$ (%)	$\Phi_{\rm r}/\Phi_{\rm r}^{~a}~(\%)$	$k_{-2} (ns^{-1})$	$\Phi_{-2a}$ (%)	$\Phi_{-2c}$ (%)	$\Phi_{\rm r}$ (%)	$\Phi_{\rm r}/\Phi_{\rm r}^{\ a}$ (%)
78	0.006	8.7	91.2	15.9					
100	0.03	34.5	65.4	11.4					
120	0.04	42.9	57.0	10.0	0.22	0.00	78.3	21.6	2.5
140	0.11	64.3	35.6	6.2					
160	0.20	76.7	23.2	4.0					
220	0.55	89.8	10.1	1.7	0.40	64.9	21.7	13.3	1.5
300	1.03	94.2	5.7	1.0	0.65	76.7	14.6	8.6	1.0
<sup>a</sup> At 300 K.									

physical contraction are temperature-independent. Significant differences in intensities and spectral shapes of the PL spectra at various temperatures can be detected. At 78 K, both exhibit a greater PL intensity owing to the suppression of nonradiative processes (Figure 2, parts a and c). The integrated PL intensities, normalized by the value at 300 K, are plotted in Figure 2e. The 100 nm film at 78 K exhibited a PL intensity enhancement of ~20x. For 5 nm thin film, only a 3x PL intensity enhancement was obtained at 78 K. The spectral shape of the 100 nm film changes dramatically, with the 0-0 vibronic peak gaining intensity relative to the 0-1 peak. This change is not observed in the 5 nm thin film. In both films, a slight red-shift of the PL spectrum is also observed from 300 to 78 K (Figure 2f). At 78 K, the PL spectrum of 100 nm film exhibits a longer peak wavelength (577 nm) than that of 5 nm case (570 nm). The different temperature dependent vibronic spectra and intensities indicate that the nanoscopic rubrene environments are different for the two different film thicknesses.

Further evidence for different exciton dynamics in the 5 and 100 nm rubrene thin films comes from TRPL experiments. TRPL measurements were conducted while varying the temperature from 78 to 300 K as shown in Figure 3, parts a and b. As the temperature decreased, the fluorescence decay of 5 and 100 nm films slowed as the nonradiative relaxation decreased. The longer-time (2  $\mu$ s) TRPL signals of all films showed delayed fluorescence, suggesting that the majority of the nonradiative decay involved SF (Figure S4). At 78 K, the TRPL signal of the 100 nm thin film showed a single exponential decay, but for all other samples, the decay was multiexponential over the 20 ns window. With increasing temperature, the TRPL decay rate became faster for all samples. In order to extract a rate constant for the Arrhenius analysis, we performed an exponential fit on the decay in the 0-2 ns window. We assumed that the fission rate,  $k_{-2}$ , was related to the total measured decay rate k by the relation  $k_{-2}$  =  $k - k_r$ , where  $k_r = 0.0625 \text{ ns}^{-1}$ , as derived from the single exponential decay of rubrene in toluene.  $k_{-2}$  at various temperatures for the 5 and 100 nm films was extracted from fitting the data in Figure 3, parts a and b, and is plotted in Figure 3c. This data can be analyzed using the Marcus nonadiabatic rate expression: 12,31

$$k_{-2} = AT^{-1/2}e^{-\Delta G_{-2}^*/k_{\rm B}T}$$
 (1)

In eq 1, A is a constant,  $\Delta G^*_{-2}$  is the activation energy, and  $k_B$  is the Boltzmann constant. By using eq 1 to fit the data in Figure 3c, a  $\Delta G^*_{-2}$  of  $58 \pm 2$  meV was obtained from the case of 100 nm film over the temperature range 300–78 K. Over the range 300–160 K, a  $\Delta G^*_{-2}$  value of 40.2  $\pm$  2 meV was

obtained for the 5 nm film. Below 160 K, the  $\Delta G^*_{-2}$  of 5 nm film was close to zero and  $k_{-2} = 0.22$  ns<sup>-1</sup> was constant.

The different behaviors of the 5 and 100 nm films can be analyzed using a simple model with rate eqs 2-4.

$$\frac{\mathrm{d}N_{S1}}{\mathrm{d}t} = -(k_r + k_{-2})N_{S1} + k_2N_{TT} \cong -(k_r + k_{-2})N_{S1},$$

$$(t < 2 \text{ ns})$$
(2)

$$N_{S1} = N_{S1}^0 e^{-(k_r + k_{-2})t} (3)$$

$$k = \frac{1}{\tau}, k_{-2} = k - k_r = (\alpha \cdot k_{-2a} + \beta \cdot k_{-2c}), \ \alpha + \beta = 1$$
(4)

$$\Phi_{-2a} = \frac{\alpha \cdot k_{-2a}}{k_r + k_{-2}}, \quad \Phi_{-2c} = \frac{\beta \cdot k_{-2c}}{k_r + k_{-2}}, \quad \Phi_r = \frac{k_r}{k_r + k_{-2}}$$
(5)

In these equations,  $N_{SD}$ ,  $N_{SO}^0$  and  $N_{TT}$  are the singlet population, initial singlet population and triplet pair population densities, respectively;  $k_r$ ,  $k_{-2}$ ,  $k_{-2a}$ ,  $k_{-2c}$  and  $k_2$  are the rates of radiative, overall SF, SF by channel a, SF by channel c, and triplet fusion, respectively. The relaxation of channel b was included in  $k_r$  because it is assumed to be fission incapable. We have focused on the SF rate on short time scales and neglected the long time triplet fusion rate  $(k_2)$  to simplify the above rate equations. k is the reciprocal of  $\tau$ , which is the singlet lifetime extracted from the TRPL signals.  $\alpha$  and  $\beta$  are the weighting factors that describe the relative fractions of excitons that undergo SF via species a and c, respectively, with the limitation of  $\alpha + \beta = 1$ .

Deduced from Figure 3b, the SF rate due to channel  $c(k_{-2c})$ was  $0.22 \text{ ns}^{-1}$  and was temperature independent.  $k_r$  was set to 0.0625 ns<sup>-1</sup>, derived from the single exponential decay of rubrene in toluene. For the 100 nm rubrene film, no sign of c was observed, so its SF rate came from channels  $a(k_{-2} = k_{-2a})$ alone. However, for the 5 nm film, the overall SF rate ( $k_{-2} = k$  $-k_r$ ) contains contributions from both channels a and c. The kinetic parameters used to fit the temperature-dependent TRPL signals in parts a and b of Figure 3 are listed in Table 1. The quantum yields for radiative decay and SF from species a and c ( $\Phi_{r}$ ,  $\Phi_{-2a}$  and  $\Phi_{-2c}$  respectively) are defined in eqs 5. At 300 K, SF via channel a dominated the fluorescence decay with over 94% exciton quenching in 100 nm film. As the temperature decreased from 300 to 78 K, the 100 nm rubrene became SF inactive, with only 8% of the excitons undergoing SF, so the PL quantum yield  $(\Phi_r)$  increased from 5.7% to 91.2%, corresponding to a 16× enhancement. This increase echoed the intensity enhancement (approximate 19.7×) seen in Figure 2c. In the 5 nm film at 300 K, 76% and 14% excitons

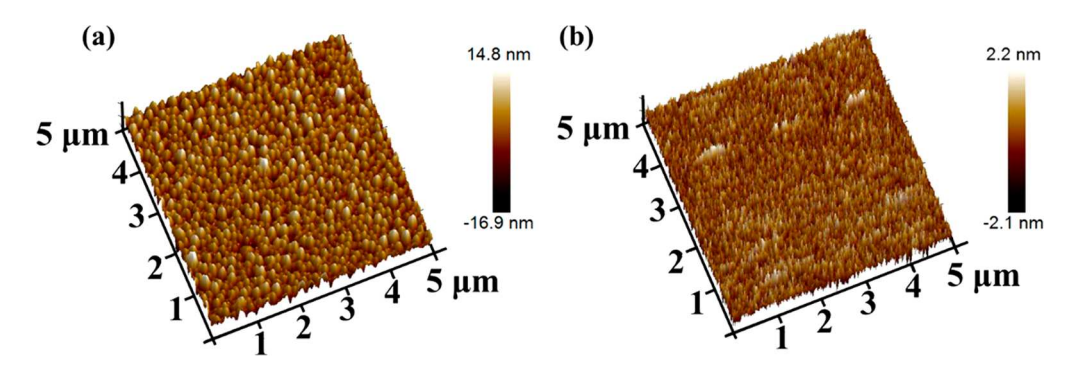


Figure 4. AFM images for (a) 5 nm rubrene thin film, and (b) 100 nm rubrene thin films.

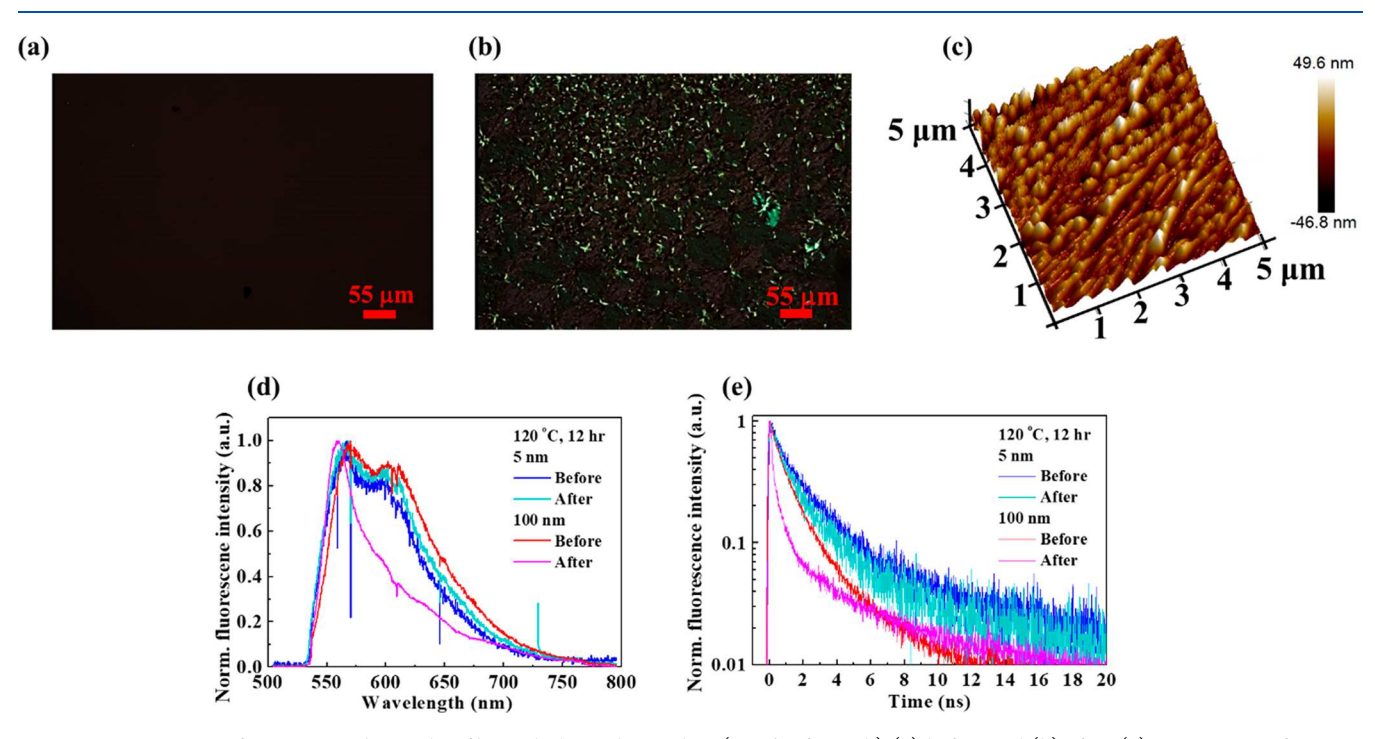


Figure 5. POM images for 100 nm rubrene thin film with thermal annealing (120  $^{\circ}$ C for 12 h) (a) before and (b) after. (c) AFM image of 100 nm rubrene after thermal annealing. (d) Steady-state PL spectra and (e) fluorescence decay (20 ns window) at T of 300 K for 5 and 100 nm films before and after thermal treatment.

undergo SF via channels a and c, respectively. At 78 K, 78.3% of singlet excitons underwent SF via channel c owing to its exothermic property for the 5 nm film. Hence,  $\Phi_r$  only showed a 2.5× enhancement relative to that at 300 K. A greater delayed fluorescence signal for the 5 nm film in the  $\mu$ s window relative to that of the 100 nm film could be observed in Figure S5. This signal originates from triplet fusion, consistent with the idea that more triplets are being produced by SF in this film.

Molecular packing determines the energetic levels and SF rates. So it is important to identify the possible PL emission species for the rubrene thin films. For the 100 nm film at 300 K, the broad emission profile can be attributed to a species that does not undergo SF. If channel a is associated with a specific type of rubrene molecule in the film, this species will not contribute the emission due to rapid SF. At 78 K, the new vibronic spectral profile suggests that channel a can be associated with a different type of rubrene that more closely resembles that seen in single crystals. The  $\Delta G^*_{-2}$  derived for channel a is similar to those measured for rubrene single crystals.<sup>32</sup> So species a might be attributed to the  $\pi$ -stacked

molecular pair, similar to that found in the orthorhombic unit cell where the molecules are separated and displaced by 3.7 and 6.1 Å, respectively.<sup>33</sup> But this species is clearly not identical with crystalline rubrene, since the absolute rate is much slower than in the single crystal, indicating that the Arrhenius prefactor A is smaller. Presumably there are also rubrene molecules without suitable neighbors for SF. The surprising thing is that a new SF channel appears in the 5 nm film that gives rise to reasonably fast, exothermic SF. We suspect this pathway is associated with sites in the film that have a greater singlet energy (30–40 meV) and a smaller SF rate than channel a. Therefore, channel c might be attributed to molecular pairs with poor  $\pi$ -stacking or partial overlap.<sup>30,34</sup>

In order to gain further insight into the structural differences between the 5 and 100 nm rubrene films, atomic force microscopy (AFM) measurements were performed (Figure 4, parts a and b). For the 5 nm rubrene thin film, Volmer—Weber or Stranski—Krastanov growth modes were observed with grain sizes around 100–200 nm. The roughness of the 5 nm rubrene film ( $R_{\rm q}=4.35$  nm) was much greater than that of 100 nm one ( $R_{\rm q}=0.604$  nm). Other rubrene films showed a rough surface

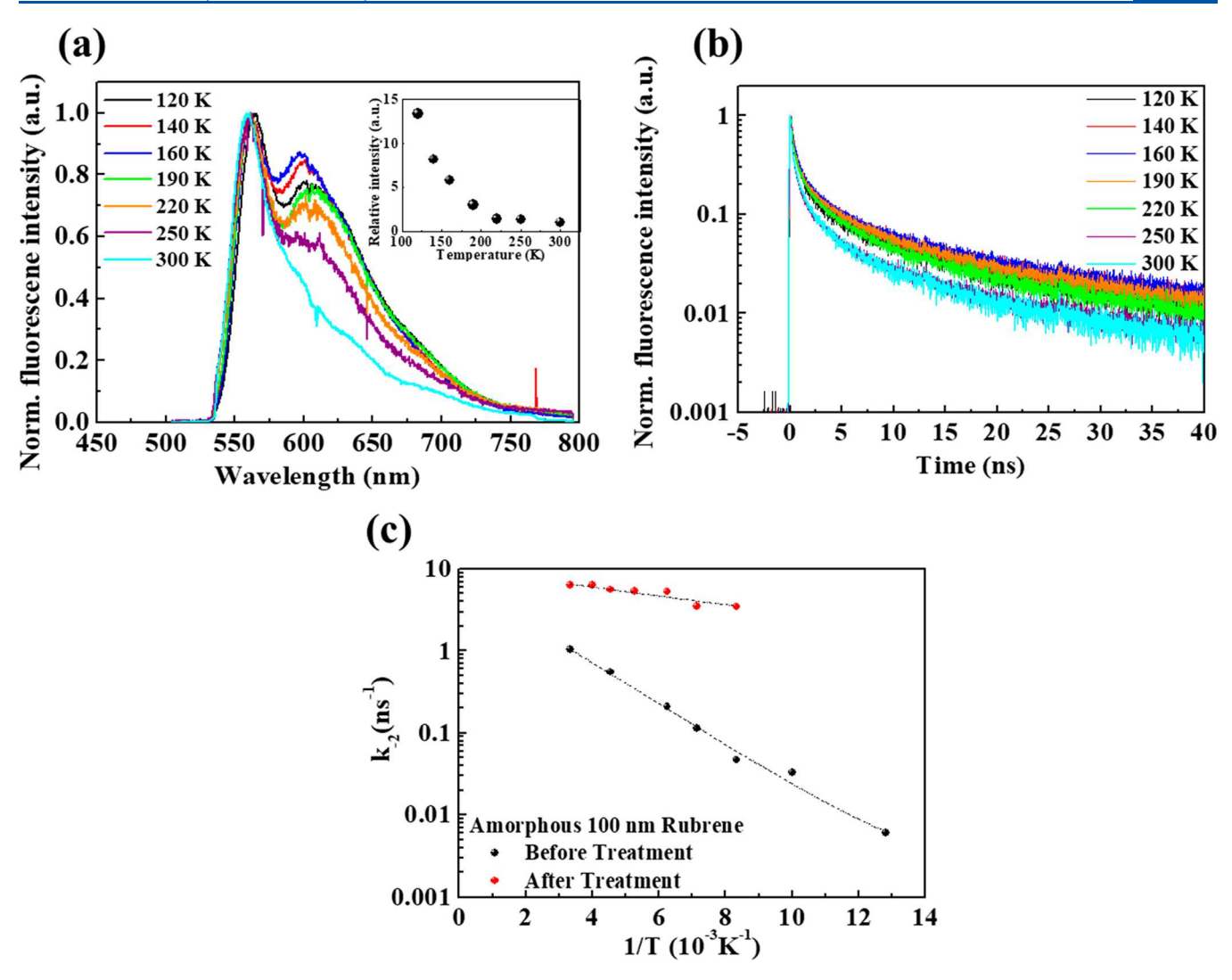


Figure 6. Temperature-dependent (a) PL spectra and (b) TRPL signals (40 ns window) for 100 nm rubrene thin film after thermal annealing, and (c) fission rates with Arrhenius plot.

profile with island distribution at the beginning of thin film growth by molecule beam deposition, which is similar to our thermal deposition process.<sup>24,31</sup> As the rubrene film became thicker, the roughness of rubrene film decreased, leading to a uniform 2D surface.

Parts a and b of Figure 5 display polarized optical microscopy (POM) images of a 100 nm rubrene film before and after thermal annealing at 120 °C for 12 h. Before thermal annealing, no crystallites could be detected in Figure 5a. After thermal annealing, spherulitic disks domains were observed in Figure 5b, indicating the phase transition from amorphous to crystalline at sites within the film. This transition is also consistent with the appearance of rubrene crystal peaks in the XRD pattern shown in the Supporting Information, Figure S1.35-37 Its AFM image also showed aggregation with directional-lamellae structures and a large roughness value  $R_0$ = 12.9 nm (Figure 5c).<sup>21</sup> On the other hand, when thermal annealing was applied to the 5 nm film, no change in phase domain and morphology could be observed from the POM and AFM images. Figure 5, parts d and e, show the PL spectra and TRPL decay curves of the 5 and 100 nm films before and after thermal annealing, respectively. For the 5 nm rubrene film, the PL spectra were almost identical. In contrast, in the

100 nm film, the PL spectrum exhibited a different spectral profile with a lower intensity around 600 nm, which was attributed to crystalline ordering of rubrene molecules with cpolarized emission. 21,28 By examining the temperature-dependent TRPL signals over the short time window of 12 ns (Figure 5e), the 5 nm film showed similar fluorescence decays before and after thermal annealing, which implied that no change in molecular packing and film conformation was induced by thermal annealing. On the contrary, temperature-dependent TRPL signals of the 100 nm film exhibited accelerated decays indicating more efficient SF, which we attribute to an increase in the density of coupled rubrene molecular pairs (SF sites) after thermal annealing. 16 In Figure S6, greater delayed fluorescence with a shorter lifetime could be observed at longer time scales ( $\mu$ s window), indicating the thermal annealing increased both SF and TF rates.

Figure 6a shows the temperature-dependent PL spectra of the annealed 100 nm film. At 300 K, only the *c*-polarized single-crystal emission was observed. However, the relative intensity around 600 nm increased with decreasing temperature, which suggests that the less crystalline regions are starting to contribute to the emission. The microscopy images suggest that most of the annealed 100 nm film is still

amorphous with small crystallites distributed within it. The more rapid singlet decays after thermal annealing probably result from rapid Förster resonance energy transfer from the amorphous regions to the crystalline regions where rapid SF is allowed. 38-40 Exciton diffusion in the amorphous regions is likely suppressed at low temperature, and hence emission from the amorphous regions can be observed more readily, as shown in the inset of Figure 6a. 41–43 The idea that excitons left in the amorphous regions avoid SF is supported by wavelength dependent TRPL experiments at 560 and 610 nm (Figure S7). All the decays have a subnanosecond initial component rapid and weak temperature dependence. This fast decay reflects excitons that undergo efficient energy transfer to the crystalline regions. Hence, the exciton dynamics within 0.5 ns is dominated by crystalline domains that receive excitons very rapidly from the surrounding film. There is also a longer-lived emission that is stronger at 610 nm than 560 nm. These redshifted excitons are the ones left behind in the amorphous regions that do not undergo rapid SF.

In Figure 6b, the diffusion mediated SF decay after thermal treatment was rapid compared to that from the 100 nm film without the thermal treatment. He annealed rubrene films, the SF process always has an average  $\Delta G^*_{-2}$  less than 10 meV (Figure 6c). We think this activation energy reflects temperature dependent diffusion in the amorphous regions, rather than the intrinsic activation energy for SF in a pure crystal.

#### CONCLUSIONS

In this paper, a surprising dependence of the exciton dynamics on rubrene film thickness was observed and investigated. In case of a 100 nm film, the exciton dynamics were dominated by channel a with an activation energy of 58 meV, which was attributed to the presence of orthorhombic rubrene crystal regions. In case of a 5 nm film, fission occurred via both the endothermic channel as well as an exothermic SF channel that may reflect a novel packing motif present only at the beginning of film deposition. Thermal annealing produced a phase transition from amorphous to polycrystalline in the 100 nm film, and this polycrystalline rubrene showed more efficient SF due to the higher density of single crystals with c-polarized order which formed SF hotspots to facilitate SF after singlet exciton diffusion. This process was weakly temperaturedependent, probably reflecting singlet exciton diffusion through the amorphous region followed by via Förster energy transfer to crystallites where rapid SF occurs.

### ASSOCIATED CONTENT

# **Supporting Information**

The Supporting Information is available free of charge at https://pubs.acs.org/doi/10.1021/acs.jpcc.0c07887.

X-ray Diffraction data, absorption and PL emission spectra and TRPL decay (PDF)

## AUTHOR INFORMATION

# **Corresponding Authors**

Tien-Lung Chiu — Department of Electrical Engineering, Yuan Ze University, Taoyuan 32003, Taiwan; orcid.org/0000-0002-0631-660X; Email: tlchiu@saturn.yzu.edu.tw

Juen-Kai Wang – Institute of Atomic and Molecular Sciences, Academia Sinica, Taipei 10617, Taiwan; Center for Condensed Matter Sciences, National Taiwan University, Taipei 10617, Taiwan; Email: jkwang@ntu.edu.tw

Jiun-Haw Lee — Graduate Institute of Photonics and Optoelectronics and Department of Electrical Engineering, National Taiwan University, Taipei 10617, Taiwan; orcid.org/0000-0003-3888-0595; Email: jiunhawlee@ntu.edu.tw

#### **Authors**

Chia-Hsun Chen – Graduate Institute of Photonics and Optoelectronics and Department of Electrical Engineering, National Taiwan University, Taipei 10617, Taiwan

Pin-Hao Sher – Institute of Atomic and Molecular Sciences, Academia Sinica, Taipei 10617, Taiwan

Cheng-Pin Chen – Graduate Institute of Photonics and Optoelectronics and Department of Electrical Engineering, National Taiwan University, Taipei 10617, Taiwan

Wing-Kit Choi – Graduate Institute of Photonics and Optoelectronics and Department of Electrical Engineering, National Taiwan University, Taipei 10617, Taiwan

Christopher J. Bardeen — Department of Chemistry, University of California, Riverside, California 92506, United States; © orcid.org/0000-0002-5755-9476

Complete contact information is available at: https://pubs.acs.org/10.1021/acs.jpcc.0c07887

## **Author Contributions**

J.-K.W. and P.-H.S. supported the TRPL system for exciton dynamics. W.-K.C. supported the POM measurement for phase transition of rubrene thin film. T.-L.C., J.-H.L., and C.J.B. directed the experiments and supervised the projects. C.-H.C. and C.-P.C. were responsible for sample preparations, TRPL measurement, and manuscript preparation.

## Notes

The authors declare no competing financial interest.

## ACKNOWLEDGMENTS

This work was supported by the Ministry of Science and Technology (MOST), Taiwan, under Grants MOST 108-2112-M-002-010-MY3, 108-2912-I-155-504-MY3, 108-2811-E-155-504, 107-2221-E-155-058-MY3, 107-2221-E-002-156-MY3, 107-2221-E-155-027, 107-3113-E-155-001-CC2, 106-3113-E-155-001-CC2, 106-2221-E-155-036, 106-2923-E-155-002-MY3, 106-2923-E-002-004-MY3, and 105-2221-E-002-130-MY3, the MEGA project, which has received funding from the European Union's Horizon 2020 research and innovation program under Marie Skłodowska-Curie Grant Agreement No. 823720. C.J.B. acknowledges support by the U.S. National Science Foundation, Grant CHE-1800187. J.K.W. acknowledges support from Academia Sinica with the project number AS-106-SS-A02.

## ABBREVIATIONS

SF, singlet fission; PV, photovoltaic; OLEDs, organic light emitting diodes; IQE, internal quantum yield; TRPL, timeresolved PL; POM, polarized optical microscopy

## REFERENCES

(1) Siebbeles, L. D. A. Organic Solar Cells: Two Electrons from One Photon. *Nat. Chem.* **2010**, *2*, 608–609.

(2) Lee, J.; Jadhav, P.; Reusswig, P. D.; Yost, S. R.; Thompson, N. J.; Congreve, D. N.; Hontz, E.; Van Voorhis, T.; Baldo, M. A. Singlet Exciton Fission Photovoltaics. *Acc. Chem. Res.* **2013**, *46*, 1300–1311.

- (3) Qiao, X.; Ma, D. Nonlinear Optoelectronic Processes in Organic Optoelectronic Devices: Triplet-Triplet Annihilation and Singlet Fission. *Mater. Sci. Eng., R* **2020**, *139*, 100519.
- (4) Smith, M. B.; Michl, J. Recent Advances in Singlet Fission. *Annu. Rev. Phys. Chem.* **2013**, *64*, 361–386.
- (5) Smith, M. B.; Michl, J. Singlet Fission. Chem. Rev. 2010, 110, 6891–6936.
- (6) Miyata, K.; Conrad-Burton, F. S.; Geyer, F. L.; Zhu, X. Y. Triplet Pair States in Singlet Fission. *Chem. Rev.* **2019**, *119*, 4261–4292.
- (7) Casanova, D. Theoretical Modeling of Singlet Fission. Chem. Rev. 2018, 118, 7164-7207.
- (8) Zhang, Y.; Forrest, S. R. Triplets Contribute to Both an Increase and Loss in Fluorescent Yield in Organic Light Emitting Diodes. *Phys. Rev. Lett.* **2012**, *108*, 267404.
- (9) Zhang, Y.; Lei, Y.; Zhang, Q.; Xiong, Z. Thermally Activated Singlet Exciton Fission Observed in Rubrene Doped Organic Films. *Org. Electron.* **2014**, *15*, 577–581.
- (10) Piland, G. B.; Burdett, J. J.; Kurunthu, D.; Bardeen, C. J. Magnetic Field Effects on Singlet Fission and Fluorescence Decay Dynamics in Amorphous Rubrene. *J. Phys. Chem. C* **2013**, *117*, 1224–1236.
- (11) Wilson, M. W. B.; Rao, A.; Johnson, K.; Gélinas, S.; di Pietro, R.; Clark, J.; Friend, R. H. Temperature-Independent Singlet Exciton Fission in Tetracene. *J. Am. Chem. Soc.* **2013**, *135*, 16680–16688.
- (12) Sher, P. H.; Chen, C. H.; Chiu, T. L.; Lin, C. F.; Wang, J. K.; Lee, J. H. Distinct Routes of Singlet Fission and Triplet Fusion: A Fluorescence Kinetic Study of Rubrene. *J. Phys. Chem. C* **2019**, *123*, 3279–3284.
- (13) Mikhnenko, O. V.; Cordella, F.; Sieval, A. B.; Hummelen, J. C.; Blom, P. W. M.; Loi, M. A. Temperature Dependence of Exciton Diffusion in Conjugated Polymers. *J. Phys. Chem. B* **2008**, *112*, 11601–11604.
- (14) Lee, T. S.; Lin, Y. L.; Kim, H.; Rand, B. P.; Scholes, G. D. Two Temperature Regimes of Triplet Transfer in the Dissociation of the Correlated Triplet Pair after Singlet Fission. *Can. J. Chem.* **2019**, *97*, 465–473.
- (15) Shizu, K.; Adachi, C.; Kaji, H. Effect of Vibronic Coupling on Correlated Triplet Pair Formation in the Singlet Fission Process of Linked Tetracene Dimers. *J. Phys. Chem. A* **2020**, *124*, 3641–3651.
- (16) Piland, G. B.; Bardeen, C. J. How Morphology Affects Singlet Fission in Crystalline Tetracene. *J. Phys. Chem. Lett.* **2015**, *6*, 1841–1846
- (17) Sutton, C.; Tummala, N. R.; Beljonne, D.; Brédas, J. L. Singlet Fission in Rubrene Derivatives: Impact of Molecular Packing. *Chem. Mater.* **2017**, 29, 2777–2787.
- (18) Park, S. W.; Hwang, J. M.; Choi, J. M.; Hwang, D. K.; Oh, M. S.; Kim, J. H.; Im, S. Rubrene Thin-Film Transistors with Crystalline and Amorphous Channels. *Appl. Phys. Lett.* **2007**, *90*, 153512.
- (19) Luo, Y.; Brun, M.; Rannou, P.; Grevin, B. Growth of Rubrene Thin Film, Spherulites and Nanowires on Sio<sub>2</sub>. *Phys. Status Solidi A* **2007**, 204, 1851–1855.
- (20) Park, S.-W.; Jeong, S. H.; Choi, J.-M.; Hwang, J. M.; Kim, J. H.; Im, S. Rubrene Polycrystalline Transistor Channel Achieved through in Situ Vacuum Annealing. *Appl. Phys. Lett.* **2007**, *91*, 033506.
- (21) Park, S.-W.; Choi, J.-M.; Lee, K. H.; Yeom, H. W.; Im, S.; Lee, Y. K. Amorphous-to-Crystalline Phase Transformation of Thin Film Rubrene. *J. Phys. Chem. B* **2010**, *114*, 5661–5665.
- (22) Lin, Y. L.; Fusella, M. A.; Kozlov, O. V.; Lin, X.; Kahn, A.; Pshenichnikov, M. S.; Rand, B. P. Morphological Tuning of the Energetics in Singlet Fission Organic Solar Cells. *Adv. Funct. Mater.* **2016**, *26*, 6489–6494.
- (23) Finton, D. M.; Wolf, E. A.; Zoutenbier, V. S.; Ward, K. A.; Biaggio, I. Routes to Singlet Exciton Fission in Rubrene Crystals and Amorphous Films. *AIP Adv.* **2019**, *9*, 095027.
- (24) Kowarik, S.; Gerlach, A.; Sellner, S.; Schreiber, F.; Pflaum, J.; Cavalcanti, L.; Konovalov, O. Anomalous Roughness Evolution of Rubrene Thin Films Observed in Real Time During Growth. *Phys. Chem. Chem. Phys.* **2006**, *8*, 1834–1836.

- (25) Zhu, H.; Jia, W.; Chen, L.; Tang, X.; Hu, Y.; Pan, R.; Deng, J.; Xiong, Z. Trap-Induced Conversion from Singlet Fission to Intersystem Crossing Via in Situ Heating of Rubrene-Based Organic Light-Emitting Diodes. *J. Mater. Chem. C* **2019**, *7*, 553–557.
- (26) Arias, D. H.; Ryerson, J. L.; Cook, J. D.; Damrauer, N. H.; Johnson, J. C. Polymorphism Influences Singlet Fission Rates in Tetracene Thin Films. *Chem. Sci.* **2016**, *7*, 1185–1191.
- (27) Piland, G. B.; Burdett, J. J.; Hung, T. Y.; Chen, P. H.; Lin, C. F.; Chiu, T. L.; Lee, J. H.; Bardeen, C. J. Dynamics of Molecular Excitons near a Semiconductor Surface Studied by Fluorescence Quenching of Polycrystalline Tetracene on Silicon. *Chem. Phys. Lett.* **2014**, *601*, 33–38.
- (28) Irkhin, P.; Ryasnyanskiy, A.; Koehler, M.; Biaggio, I. Absorption and Photoluminescence Spectroscopy of Rubrene Single Crystals. *Phys. Rev. B: Condens. Matter Mater. Phys.* **2012**, *86*, 085143.
- (29) Gieseking, B.; Schmeiler, T.; Müller, B.; Deibel, C.; Engels, B.; Dyakonov, V.; Pflaum, J. Effects of Characteristic Length Scales on the Exciton Dynamics in Rubrene Single Crystals. *Phys. Rev. B: Condens. Matter Mater. Phys.* **2014**, *90*, 205305.
- (30) Paraskar, A. S.; Reddy, A. R.; Patra, A.; Wijsboom, Y. H.; Gidron, O.; Shimon, L. J. W.; Leitus, G.; Bendikov, M. Rubrenes: Planar and Twisted. *Chem. Eur. J.* **2008**, *14*, 10639–10647.
- (31) Yost, S. R.; et al. A Transferable Model for Singlet-Fission Kinetics. *Nat. Chem.* **2014**, *6*, 492–497.
- (32) Ma, L.; Zhang, K.; Kloc, C.; Sun, H.; Michel-Beyerle, M. E.; Gurzadyan, G. G. Singlet Fission in Rubrene Single Crystal: Direct Observation by Femtosecond Pump-Probe Spectroscopy. *Phys. Chem. Phys.* **2012**, *14*, 8307–8312.
- (33) Huang, L.; Liao, Q.; Shi, Q.; Fu, H.; Ma, J.; Yao, J. Rubrene Micro-Crystals from Solution Routes: Their Crystallography, Morphology and Optical Properties. *J. Mater. Chem.* **2010**, *20*, 159–166.
- (34) Kytka, M.; Gisslen, L.; Gerlach, A.; Heinemeyer, U.; Kováč, J.; Scholz, R.; Schreiber, F. Optical Spectra Obtained from Amorphous Films of Rubrene: Evidence for Predominance of Twisted Isomer. *J. Chem. Phys.* **2009**, *130*, 214507.
- (35) Hsu, C. H.; Deng, J.; Staddon, C. R.; Beton, P. H. Growth Front Nucleation of Rubrene Thin Films for High Mobility Organic Transistors. *Appl. Phys. Lett.* **2007**, *91*, 193505.
- (36) Wang, L.; Li, Y.; Zou, F.; Du, H.; Sun, L.; Zhang, J.; Song, X.; Song, G. Insight into Crystallization Process of Rubrene by Binary Solvent Mixtures. *RSC Adv.* **2016**, *6*, 3532–3538.
- (37) Liu, D.; Li, Z.; He, Z.; Xu, J.; Miao, Q. Induced Crystallization of Rubrene with Diazapentacene as the Template. *J. Mater. Chem.* **2012**, 22, 4396–4400.
- (38) Irkhin, P.; Biaggio, I. Direct Imaging of Anisotropic Exciton Diffusion and Triplet Diffusion Length in Rubrene Single Crystals. *Phys. Rev. Lett.* **2011**, *107*, 017402.
- (39) Najafov, H.; Lee, B.; Zhou, Q.; Feldman, L. C.; Podzorov, V. Observation of Long-Range Exciton Diffusion in Highly Ordered Organic Semiconductors. *Nat. Mater.* **2010**, *9*, 938–943.
- (40) Shim, J. H.; Raman, K. V.; Park, Y. J.; Santos, T. S.; Miao, G. X.; Satpati, B.; Moodera, J. S. Large Spin Diffusion Length in an Amorphous Organic Semiconductor. *Phys. Rev. Lett.* **2008**, *100*, 226603.
- (41) Vaubel, G.; Baessler, H. Diffusion of Singlet Excitons in Tetracene Crystals. *Mol. Cryst. Liq. Cryst.* **1970**, *12*, 47–56.
- (42) Mikhnenko, O. V.; Blom, P. W. M.; Nguyen, T. Q. Exciton Diffusion in Organic Semiconductors. *Energy Environ. Sci.* **2015**, *8*, 1867–1888.
- (43) Zhu, T.; Wan, Y.; Guo, Z.; Johnson, J.; Huang, L. Two Birds with One Stone: Tailoring Singlet Fission for Both Triplet Yield and Exciton Diffusion Length. *Adv. Mater.* **2016**, *28*, 7539–7547.
- (44) Biaggio, I.; Irkhin, P. Extremely Efficient Exciton Fission and Fusion and Its Dominant Contribution to the Photoluminescence Yield in Rubrene Single Crystals. *Appl. Phys. Lett.* **2013**, *103*, 263301.